

# Photothermal optical lock-in optical coherence tomography for *in vivo* imaging

Jason M. Tucker-Schwartz,<sup>1</sup> Maryse Lapierre-Landry,<sup>1</sup> Chetan A. Patil,<sup>1,2</sup>  
and Melissa C. Skala<sup>1,\*</sup>

<sup>1</sup>Department of Biomedical Engineering, Vanderbilt University, Nashville, TN 37235, USA

<sup>2</sup>Current address: Department of Bioengineering, Temple University, Philadelphia, PA 19122, USA  
[m.skala@vanderbilt.edu](mailto:m.skala@vanderbilt.edu)

**Abstract:** Photothermal OCT (PTOCT) provides high sensitivity to molecular targets in tissue, and occupies a spatial imaging regime that is attractive for small animal imaging. However, current implementations of PTOCT require extensive temporal sampling, resulting in slow frame rates and a large data burden that limit its *in vivo* utility. To address these limitations, we have implemented optical lock-in techniques for photothermal optical lock-in OCT (poli-OCT), and demonstrated the *in vivo* imaging capabilities of this approach. The poli-OCT signal was assessed in tissue-mimicking phantoms containing indocyanine green (ICG), an FDA approved small molecule that has not been previously imaged *in vivo* with PTOCT. Then, the effects of *in vivo* blood flow and motion artifact were assessed and attenuated, and *in vivo* poli-OCT was demonstrated with both ICG and gold nanorods as contrast agents. Experiments revealed that poli-OCT signals agreed with optical lock-in theory and the bio-heat equation, and the system exhibited shot noise limited performance. In phantoms containing biologically relevant concentrations of ICG (1  $\mu\text{g/ml}$ ), the poli-OCT signal was significantly greater than control phantoms ( $p < 0.05$ ), demonstrating sensitivity to small molecules. Finally, *in vivo* poli-OCT of ICG identified the lymphatic vessels in a mouse ear, and also identified low concentrations (200 pM) of gold nanorods in subcutaneous injections at frame rates ten times faster than previously reported. This work illustrates that future *in vivo* molecular imaging studies could benefit from the improved acquisition and analysis times enabled by poli-OCT.

©2015 Optical Society of America

**OCIS codes:** (110.4500) Optical coherence tomography; (350.5340) Photothermal effects.

## References and links

1. M. de Jong, J. Essers, and W. M. van Weerden, "Imaging preclinical tumour models: improving translational power," *Nat. Rev. Cancer* **14**(7), 481–493 (2014).
2. J. K. Willmann, N. van Bruggen, L. M. Dinkelborg, and S. S. Gambhir, "Molecular imaging in drug development," *Nat. Rev. Drug Discov.* **7**(7), 591–607 (2008).
3. A. J. Walsh, R. S. Cook, H. C. Manning, D. J. Hicks, A. Lafontant, C. L. Arteaga, and M. C. Skala, "Optical Metabolic Imaging Identifies Glycolytic Levels, Subtypes, and Early-Treatment Response in Breast Cancer," *Cancer Res.* **73**(20), 6164–6174 (2013).
4. G. M. Thurber, K. S. Yang, T. Reiner, R. H. Kohler, P. Sorger, T. Mitchison, and R. Weissleder, "Single-cell and subcellular pharmacokinetic imaging allows insight into drug action *in vivo*," *Nat. Commun.* **4**, 1504 (2013).
5. W. Drexler and J. G. Fujimoto, *Optical Coherence Tomography: Technology and Applications* (Springer, 2008).
6. T. Klein, W. Wieser, L. Reznicek, A. Neubauer, A. Kampik, and R. Huber, "Multi-MHz retinal OCT," *Biomed. Opt. Express* **4**(10), 1890–1908 (2013).
7. A. Mariampillai, B. A. Standish, E. H. Moriyama, M. Khurana, N. R. Munce, M. K. K. Leung, J. Jiang, A. Cable, B. C. Wilson, I. A. Vitkin, and V. X. D. Yang, "Speckle variance detection of microvasculature using swept-source optical coherence tomography," *Opt. Lett.* **33**(13), 1530–1532 (2008).
8. G. Liu, A. J. Lin, B. J. Tromberg, and Z. Chen, "A comparison of Doppler optical coherence tomography methods," *Biomed. Opt. Express* **3**(10), 2669–2680 (2012).
9. M. C. Skala, M. J. Crow, A. Wax, and J. A. Izatt, "Photothermal optical coherence tomography of epidermal growth factor receptor in live cells using immunotargeted gold nanospheres," *Nano Lett.* **8**(10), 3461–3467 (2008).

10. D. C. Adler, S. W. Huang, R. Huber, and J. G. Fujimoto, "Photothermal detection of gold nanoparticles using phase-sensitive optical coherence tomography," *Opt. Express* **16**(7), 4376–4393 (2008).
11. J. M. Tucker-Schwartz, T. A. Meyer, C. A. Patil, C. L. Duvall, and M. C. Skala, "In vivo photothermal optical coherence tomography of gold nanorod contrast agents," *Biomed. Opt. Express* **3**(11), 2881–2895 (2012).
12. Y. Jung, R. Reif, Y. Zeng, and R. K. Wang, "Three-dimensional high-resolution imaging of gold nanorods uptake in sentinel lymph nodes," *Nano Lett.* **11**(7), 2938–2943 (2011).
13. C. Zhou, T. H. Tsai, D. C. Adler, H. C. Lee, D. W. Cohen, A. Mondelblatt, Y. Wang, J. L. Connolly, and J. G. Fujimoto, "Photothermal optical coherence tomography in ex vivo human breast tissues using gold nanoshells," *Opt. Lett.* **35**(5), 700–702 (2010).
14. A. Nahas, M. Varna, E. Fort, and A. C. Boccara, "Detection of plasmonic nanoparticles with full field-OCT: optical and photothermal detection," *Biomed. Opt. Express* **5**(10), 3541–3546 (2014).
15. J. M. Tucker-Schwartz, T. Hong, D. C. Colvin, Y. Xu, and M. C. Skala, "Dual-modality photothermal optical coherence tomography and magnetic-resonance imaging of carbon nanotubes," *Opt. Lett.* **37**(5), 872–874 (2012).
16. B. Yin, R. V. Kuranov, A. B. McElroy, S. Kazmi, A. K. Dunn, T. Q. Duong, and T. E. Milner, "Dual-wavelength photothermal optical coherence tomography for imaging microvasculature blood oxygen saturation," *J. Biomed. Opt.* **18**(5), 056005 (2013).
17. J. M. Tucker-Schwartz, K. R. Beavers, W. W. Sit, A. T. Shah, C. L. Duvall, and M. C. Skala, "In vivo imaging of nanoparticle delivery and tumor microvasculature with multimodal optical coherence tomography," *Biomed. Opt. Express* **5**(6), 1731–1743 (2014).
18. L. Cognet, C. Tardin, D. Boyer, D. Choquet, P. Tamarat, and B. Lounis, "Single metallic nanoparticle imaging for protein detection in cells," *Proc. Natl. Acad. Sci. U.S.A.* **100**(20), 11350–11355 (2003).
19. C. Pache, N. L. Bocchio, A. Bouwens, M. Villiger, C. Berclaz, J. Goulley, M. I. Gibson, C. Santschi, and T. Lasser, "Fast three-dimensional imaging of gold nanoparticles in living cells with photothermal optical lock-in Optical Coherence Microscopy," *Opt. Express* **20**(19), 21385–21399 (2012).
20. W. J. Eldridge, A. Meiri, A. Sheinfeld, M. T. Rinehart, and A. Wax, "Fast wide-field photothermal and quantitative phase cell imaging with optical lock-in detection," *Biomed. Opt. Express* **5**(8), 2517–2525 (2014).
21. M. Wojtkowski, V. Srinivasan, T. Ko, J. Fujimoto, A. Kowalczyk, and J. Duker, "Ultrahigh-resolution, high-speed, Fourier domain optical coherence tomography and methods for dispersion compensation," *Opt. Express* **12**(11), 2404–2422 (2004).
22. S. Moon, S. W. Lee, and Z. Chen, "Reference spectrum extraction and fixed-pattern noise removal in optical coherence tomography," *Opt. Express* **18**(24), 24395–24404 (2010).
23. A. Oldenburg, F. Toubian, K. Suslick, A. Wei, and S. Boppart, "Magnetomotive contrast for in vivo optical coherence tomography," *Opt. Express* **13**(17), 6597–6614 (2005).
24. R. Leitgeb, C. Hitzenberger, and A. Fercher, "Performance of fourier domain vs. time domain optical coherence tomography," *Opt. Express* **11**(8), 889–894 (2003).
25. M. J. C. van Gemert, G. W. Lucassen, and A. J. Welch, "Time constants in thermal laser medicine: II. Distributions of time constants and thermal relaxation of tissue," *Phys. Med. Biol.* **41**(8), 1381–1399 (1996).
26. T. Hoshida, N. Isaka, J. Hagendoorn, E. di Tomaso, Y. L. Chen, B. Pytowski, D. Fukumura, T. P. Padera, and R. K. Jain, "Imaging steps of lymphatic metastasis reveals that vascular endothelial growth factor-C increases metastasis by increasing delivery of cancer cells to lymph nodes: therapeutic implications," *Cancer Res.* **66**(16), 8065–8075 (2006).
27. J. L. Li, C. C. Goh, J. L. Keeble, J. S. Qin, B. Roediger, R. Jain, Y. Wang, W. K. Chew, W. Weninger, and L. G. Ng, "Intravital multiphoton imaging of immune responses in the mouse ear skin," *Nat. Protoc.* **7**(2), 221–234 (2012).
28. W. W. Kilarski, E. Güç, J. C. M. Teo, S. R. Oliver, A. W. Lund, and M. A. Swartz, "Intravital immunofluorescence for visualizing the microcirculatory and immune microenvironments in the mouse ear dermis," *PLoS ONE* **8**(2), e57135 (2013).
29. S. Yousefi, J. Qin, Z. Zhi, and R. K. Wang, "Label-free optical lymphangiography: development of an automatic segmentation method applied to optical coherence tomography to visualize lymphatic vessels using Hessian filters," *J. Biomed. Opt.* **18**(8), 86004 (2013).
30. N. L. Harvey, R. S. Srinivasan, M. E. Dillard, N. C. Johnson, M. H. Witte, K. Boyd, M. W. Sleeman, and G. Oliver, "Lymphatic vascular defects promoted by Prox1 haploinsufficiency cause adult-onset obesity," *Nat. Genet.* **37**(10), 1072–1081 (2005).
31. S. Kwon, G. D. Agollah, W. Chan, and E. M. Sevick-Muraca, "Altered lymphatic function and architecture in salt-induced hypertension assessed by near-infrared fluorescence imaging," *J. Biomed. Opt.* **17**(8), 080504 (2012).
32. S. Kwon and E. M. Sevick-Muraca, "Mouse phenotyping with near-infrared fluorescence lymphatic imaging," *Biomed. Opt. Express* **2**(6), 1403–1411 (2011).
33. C. V. Pastuskovas, E. E. Mundo, S. P. Williams, T. K. Nayak, J. Ho, S. Ulufatu, S. Clark, S. Ross, E. Cheng, K. Parsons-Reponte, G. Cain, M. Van Hoy, N. Majidy, S. Bheddah, J. dela Cruz Chuh, K. R. Kozak, N. Lewin-Koh, P. Nauka, D. Bumbaca, M. Sliwkowski, J. Tibbitts, F. P. Theil, P. J. Fielder, L. A. Khawli, and C. A. Boswell, "Effects of anti-VEGF on pharmacokinetics, biodistribution, and tumor penetration of trastuzumab in a preclinical breast cancer model," *Mol. Cancer Ther.* **11**(3), 752–762 (2012).
34. S. I. J. Ellenbroek and J. van Rhee, "Imaging hallmarks of cancer in living mice," *Nat. Rev. Cancer* **14**(6), 406–418 (2014).
35. E. C. Dreaden, L. A. Austin, M. A. Mackey, and M. A. El-Sayed, "Size matters: gold nanoparticles in targeted cancer drug delivery," *Ther. Deliv.* **3**(4), 457–478 (2012).

36. H. Y. Lee, P. D. Raphael, J. Park, A. K. Ellerbee, B. E. Applegate, and J. S. Oghalai, "Noninvasive in vivo imaging reveals differences between tectorial membrane and basilar membrane traveling waves in the mouse cochlea," *Proc. Natl. Acad. Sci. U.S.A.* **112**(10), 3128–3133 (2015).
37. R. K. K. Wang, "In vivo full range complex Fourier domain optical coherence tomography," *Appl. Phys. Lett.* **90**(5), 054103 (2007).
38. M. Szkulmowski, I. Grulkowski, D. Szlag, A. Szkulmowska, A. Kowalczyk, and M. Wojtkowski, "Flow velocity estimation by complex ambiguity free joint Spectral and Time domain Optical Coherence Tomography," *Opt. Express* **17**(16), 14281–14297 (2009).
39. D. Boyer, P. Tamarat, A. Maali, B. Lounis, and M. Orrit, "Photothermal imaging of nanometer-sized metal particles among scatterers," *Science* **297**(5584), 1160–1163 (2002).
40. J. M. Schmitt and S. H. Xiang, "Cross-polarized backscatter in optical coherence tomography of biological tissue," *Opt. Lett.* **23**(13), 1060–1062 (1998).
41. P. Lenton, J. Rudney, R. Chen, A. Fok, C. Aparicio, and R. S. Jones, "Imaging in vivo secondary caries and ex vivo dental biofilms using cross-polarization optical coherence tomography," *Dent. Mater.* **28**(7), 792–800 (2012).
42. R. S. Jones and D. Fried, "Remineralization of enamel caries can decrease optical reflectivity," *J. Dent. Res.* **85**(9), 804–808 (2006).
43. G. Guan, R. Reif, Z. Huang, and R. K. Wang, "Depth profiling of photothermal compound concentrations using phase sensitive optical coherence tomography," *J. Biomed. Opt.* **16**(12), 126003 (2011).
44. S. D. Perrault, C. Walkey, T. Jennings, H. C. Fischer, and W. C. W. Chan, "Mediating Tumor Targeting Efficiency of Nanoparticles Through Design," *Nano Lett.* **9**(5), 1909–1915 (2009).
45. L. Tang, T. M. Fan, L. B. Borst, and J. Cheng, "Synthesis and Biological Response of Size-Specific, Monodisperse Drug-Silica Nanoconjugates," *ACS Nano* **6**(5), 3954–3966 (2012).
46. Y. Akiyama, T. Mori, Y. Katayama, and T. Niidome, "The effects of PEG grafting level and injection dose on gold nanorod biodistribution in the tumor-bearing mice," *J. Control. Release* **139**(1), 81–84 (2009).
47. M. M. Arida, M. M. Janat-Amsbury, A. Ray, C. M. Peterson, and H. Ghandehari, "Geometry and surface characteristics of gold nanoparticles influence their biodistribution and uptake by macrophages," *Eur. J. Pharm. Biopharm.* **77**(3), 417–423 (2011).
48. S. W. Jones, R. A. Roberts, G. R. Robbins, J. L. Perry, M. P. Kai, K. Chen, T. Bo, M. E. Napier, J. P. Y. Ting, J. M. Desimone, and J. E. Bear, "Nanoparticle clearance is governed by Th1/Th2 immunity and strain background," *J. Clin. Invest.* **123**(7), 3061–3073 (2013).
49. K. M. Poole, C. E. Nelson, R. V. Joshi, J. R. Martin, M. K. Gupta, S. C. Haws, T. E. Kavanaugh, M. C. Skala, and C. L. Duvall, "ROS-responsive microspheres for on demand antioxidant therapy in a model of diabetic peripheral arterial disease," *Biomaterials* **41**, 166–175 (2015).
50. C. E. Nelson, A. J. Kim, E. J. Adolph, M. K. Gupta, F. Yu, K. M. Hocking, J. M. Davidson, S. A. Guelcher, and C. L. Duvall, "Tunable delivery of siRNA from a biodegradable scaffold to promote angiogenesis in vivo," *Adv. Mater.* **26**(4), 607–614 (2014).

## 1. Introduction

*In vivo* molecular imaging in animal models serves a vital role in medical research, providing fundamental insights into mechanisms of disease formation and progression [1], as well as drug discovery [2]. Unfortunately, current small animal molecular imaging tools supply either high resolution or a wide field of view, but not both. For example, fluorescence microscopy can image molecular contrast *in vivo* [3, 4] at subcellular ( $<1\ \mu\text{m}$ ) resolution, but only over a small, depth-limited field of view of a few hundred micrometers. Unlike microscopy, whole body imaging (e.g. bioluminescence imaging, positron emission tomography, magnetic resonance imaging) of contrast agents provide molecular images without practical limitations to imaging depth. However, whole body imaging approaches suffer from limited spatial resolution (mm-cm) [2]. Optical coherence tomography (OCT) fills the niche of high resolution (1-30  $\mu\text{m}$ ), wide field of view (5-10 mm), and deep (1-3 mm) three-dimensional optical imaging [5]. OCT is a cost-effective noncontact imaging tool, capable of MHz line rates [6]. Using low coherence interferometry of near infrared (NIR) photons, OCT provides depth-resolved images of tissue structure, vessel morphology [7], and blood flow [8]. Yet, OCT is not especially sensitive to molecular targets, since the index of refraction varies weakly amongst most molecular species in tissue.

Photothermal OCT (PTOCT), a functional extension of OCT, enhances the sensitivity and specificity of OCT to molecular sources of contrast [9, 10]. Similar to photoacoustic imaging, another emerging molecular imaging technique, PTOCT images the effects of photon absorption. Unlike photoacoustic imaging, PTOCT is a contact-free tool that images heat release after photon absorption, rather than the release of acoustic waves from thermally confined laser pulses. After photon absorption by a chromophore, heat released into the

microenvironment causes thermoelastic expansion and slight changes in local refractive index, which in turn alter the observed optical path length. PTOCT quantifies these photothermal-induced optical path length variations using phase-sensitive OCT measurements and post-acquisition frequency analysis. PTOCT has been used to image a range of exogenous and endogenous forms of contrast *in vitro* and *ex vivo* including gold nanospheres [9], gold nanorods [11, 12], gold nanoshells [10, 13, 14], carbon nanotubes [15], and blood [16]. Recently, PTOCT was expanded to *in vivo* applications, and used to track *in vivo* heterogeneities in intratumoral nanoparticle distributions [17]. Even with its recent success, PTOCT still suffers from impracticalities that limit its widespread use for *in vivo* molecular imaging. In the traditional PTOCT implementation for imaging trace concentrations of contrast agents, one A-scan position is temporally sampled hundreds to thousands of times, and heating dynamics are identified from the phase of the depth-resolved OCT signal using post-acquisition frequency analysis. This post-acquisition frequency analysis scheme requires time consuming data acquisition, excessive data collection, and lengthy offline signal analysis. These limitations make traditional PTOCT impractical and lengthy for multi-animal *in vivo* time-course studies, and have therefore restricted its use in research.

Optical lock-in detection, a real-time alternative to post-acquisition frequency analysis, has been previously implemented for photothermal microscopy of cell monolayers [18]. This approach was recently expanded to depth-resolved photothermal optical coherence microscopy [19] and two-dimensional wide field photothermal microscopy [20] of gold nanospheres in cell monolayers. Specifically, a photothermal optical lock-in optical coherence microscopy (poli-OCM) technique was developed, allowing for kHz line rate photothermal imaging with OCM systems [19]. By imposing a frequency shift on the reference arm light, this optical lock-in technique removes the temporal sampling constraints of photothermal OCM, thus reducing its data burden and effectively transforming the OCM signal to a real time image of photothermal heating. However, optical lock-in acquisition has yet to be demonstrated in optically thick samples or *in vivo*, where confounding factors such as motion and blood flow introduce artifacts into the image.

Here, optical lock-in techniques are implemented for real time imaging of NIR absorbing contrast agents *in vivo* using photothermal optical lock-in optical coherence tomography (poli-OCT). An *in vivo* poli-OCT system was built and tested using tissue-mimicking phantoms. In addition, motion artifact and blood flow, which are confounding factors unique to *in vivo* imaging, were characterized and attenuated. Finally, contrast agents were imaged *in vivo* using frame rates at least 10 fold faster than previous *in vivo* publications [11, 17]. Two contrast agents were imaged *in vivo* in order to demonstrate the versatility of poli-OCT to a range of contrast agents, including an FDA approved small molecule (indocyanine green: ICG) that has not been previously measured *in vivo* with PTOCT, as well as gold nanorods. Overall, the development of poli-OCT for *in vivo* use provides improved *in vivo* molecular imaging in the unique spatial niche of OCT.

## 2. Materials and methods

### 2.1. poli-OCT imaging

The theory for poli-OCT has previously been published [19]. In an interferometric imaging system, a carrier frequency is introduced by imposing a temporal frequency shift ( $\Omega_R$ ) onto the reference arm. In the presence of photon-absorbing molecules and frequency matched photothermal-induced phase oscillations ( $\Omega_P$ ), the resulting interference pattern is demodulated. Low pass filtering then distinguishes the demodulated signal from background. Temporal integration by the CCD serves as the low pass filter, attenuating the signal due to static scatterers to zero, and maintaining the demodulated signal due to absorption (Fig. 1(a)). To attenuate the signal due to scatterers, the integration time ( $\tau$ ) of the CCD must be set to a multiple ( $n$ ) of the frequency shift period ( $T_0$ , where  $\tau = n/\Omega_R = nT_0$ ). This optical lock-in technique transforms the OCT signal as a function of depth ( $z$ ), defined as the amplitude of the tomogram ( $|S(z)|$ ) after Fourier transform of the interference signal, to a real time image of

photothermal heating (i.e. poli-OCT). The poli-OCT signal at a given depth ( $|S(z)|$ ) where an absorber such as ICG is present is described by

$$|S(z)| \propto \alpha \tau r(z) r_r \sqrt{P_s P_r} \quad (1)$$

where  $\alpha$  describes the magnitude of the photothermal heating signal,  $r(z)$  and  $r_r$  are the reflectivities at depth  $z$  in the sample and at the reference arm, respectively and  $P_s$  and  $P_r$  are the power to the sample and reference arm, respectively [19].

For *in vivo* imaging, a custom poli-OCT system was constructed with an 860 nm center wavelength, 40 nm bandwidth (Fig. 1(b), yellow, inset), superluminescent diode imaging laser (SLD, Fig. 1(b)). Light from the SLD was split between the sample and reference arms using a 50:50 fiber coupler (50:50, Fig. 1b). A programmable frequency shift ( $\Omega_R$ ) was applied to the reference arm using the beat frequency of two acousto-optic modulators (AOMs) in serial configuration. The first AOM (AOM 1, Fig. 1(b)) performed a frequency downshift at the AOM central carrier frequency ( $\omega_c$ , where  $\omega_c = 100$  MHz), while the second AOM (AOM 2, Fig. 1(b)) performed a slightly offset frequency upshift ( $\omega_c + \Omega_R$ ). AOMs operate on the MHz time scale, therefore the beat frequency ( $\Omega_R$ ) of AOM 1 and AOM 2 was used to shift the operational range to the Hz and kHz regime, where photothermal effects are large enough to image with our focused spot size (24  $\mu$ m). A custom phase-locked AOM driver (Brimrose) controlled the frequency shifts and power throughput of both AOMs, with an operational range of 80-120 MHz and 1 Hz resolution. Knife edges removed zeroth-order output beams from the AOMs, and the reference arm light was focused into a fiber coupler for interferometry. In the sample arm, polarization optics were used to control power to the sample and minimize autocorrelation artifacts. Light output from the 50:50 fiber coupler was collimated and the polarization angle was tuned using a half wave plate (HWP, Fig. 1(b)). A linear polarizer (LP, Fig. 1(b)) then rejected any light off axis from the reflective mode of the polarization beam splitter (PBS, Fig. 1(b)). After reflection towards the sample by the PBS, a quarter wave plate (QWP, Fig. 1(b)) controlled the polarization shape of the sample arm light, from circular (45 degrees) to linear (0 degrees). A 3X scan lens (Thorlabs) then focused the light onto the sample (depth of field = 1.15 mm,  $1/e^2$  spot size = 24  $\mu$ m). Any light backreflected from the sample that matched the transmission state of the PBS was collected into a fiber coupler for interferometry. The output interference signal from the fiber coupler was dispersed by a spectrometer and captured by a CCD with tunable integration time from 50 to 10,000  $\mu$ s. To achieve optical lock-in detection, the integration time ( $\tau$ ) of the CCD was set to a multiple ( $n$ ) of the frequency shift period ( $T_0$ , where  $\tau = n/\Omega_R = nT_0$ ). The spectrometer, galvo drive electronics, and software from a commercial OCT system (BiopTigen) were used for the poli-OCT system.

Photothermal heating was achieved with a wavelength tunable Titanium:Sapphire (Fig. 1(b)) photothermal laser (PT laser). The wavelength of the PT laser (Fig. 1(b), green, inset) was tuned to match the absorption of the selected contrast agent, as shown for ICG (Fig. 1(b), inset). To induce photothermal phase oscillations, the PT laser was intensity modulated at the same frequency as the reference arm ( $\Omega_P$ , where  $\Omega_P = \Omega_R$ ) using a third AOM (AOM 3, Fig. 1(b)), and then fiber coupled into the imaging system. Commercial software (Brimrose) controlled the frequency shifts in all three AOMs, while analog inputs (0-1 V) drove the intensity of the output RF signal. The RF signals sent to AOM 1 and AOM 2 were attenuated, mixed, and then low pass filtered using inline RF electronics to isolate the beat waveform. The beat waveform from AOM 1 and AOM 2 was digitally acquired, conditioned in LabVIEW to a square wave frequency matched to the beat of AOMs 1 and 2 ( $\Omega_P = \Omega_R$ ), and output as an analog waveform to intensity modulate AOM 3.

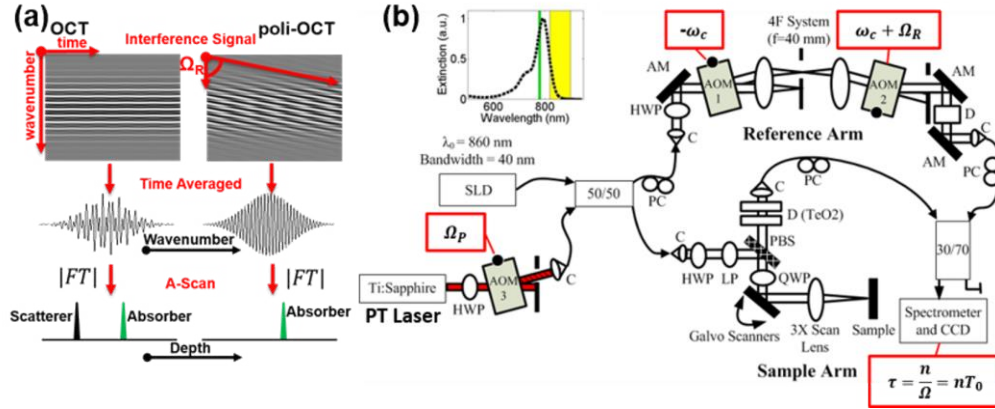


Fig. 1. Photothermal optical lock-in OCT. (a) In poli-OCT, a frequency shift ( $\Omega_R$ ) is imposed on the reference arm, which attenuates time-averaged interference signals from static non-absorbing samples. (b) A custom poli-OCT system was constructed for *in vivo* imaging. ICG (extinction spectrum, inset) was heated using 770 nm light (green, inset) from the Ti:Sapphire photothermal laser (PT laser). An 860 nm wavelength, 40 nm bandwidth, superluminescent diode (SLD) was used for imaging (yellow, inset). D (TeO<sub>2</sub>): Dispersion matching of AOM crystals; D: Dispersion compensation; HWP: Half wave plate; LP: Linear polarizer; QWP: Quarter wave plate; PBS: Polarization sensitive beam splitter; AOM: Acousto-optic modulator; SLD: Superluminescent diode; C: Fiber collimation/coupling; AM: Alignment mirror; PC: Polarization controller

## 2.2. Image processing

Unlike traditional PTOCT which requires Fourier analysis of the digitally sampled temporal phase data [11], poli-OCT images require the same image processing as standard OCT images. If the instrumentation and signal requirements are met, either an OCT ( $\Omega_R = 0$  Hz) or poli-OCT ( $\Omega_R \neq 0$  Hz and  $\Omega_R = n/\tau$ ) image are acquired. To process images, data was first resampled from linearity in wavelength to linearity in wavenumber. The interference spectrum was then numerically dispersion corrected [21], followed by a Fourier transform along the wavenumber dimension to create the depth-resolved image. Fixed pattern noise removal was performed on the complex signal [22], and the poli-OCT signal was calculated as the non-log compressed magnitude of the depth-resolved data.

## 2.3. Imaging of phantoms

To quantify system performance and optimize the system for *in vivo* imaging, scattering phantoms were imaged with poli-OCT under varying parameters. Tissue mimicking phantoms containing ICG for photothermal absorption were created from clear silicone (Quantum Silicones) consisting of two parts (A and B) mixed at a 10:1 weight ratio. Rutile titanium dioxide (TiO<sub>2</sub>, Sigma Aldrich) was added to a final concentration of 4.1 mg/g to mimic human skin scattering [23]. The TiO<sub>2</sub> was added to silicone component A, mixed for two minutes, and then degassed for two minutes using a planetary centrifugal mixer (Thinky USA). ICG diluted into a small volume of 70% ethanol was added to component B of the silicone mixture to a final concentration of 8  $\mu$ g/ml, then mixed and degassed. Components A and B were then mixed and degassed. The final mixture was placed in a petri dish under vacuum at 29 inches of Hg for five minutes with brief returns to standard pressure every minute, and left to cure for 12 hours at 70 degree Celsius. Phantoms were imaged using a 2 mm B-scan (400 A-scans/B-scan) and data was averaged across each B-scan including the first 400  $\mu$ m in depth in the phantom. Baseline acquisition parameters for phantom studies were 500  $\mu$ W of SLD sample arm power, 25 mW average PT laser power to the sample, 6 ms CCD integration time, and 500 Hz frequency shift ( $\Omega_P = \Omega_R$ ). In addition, reference arm power was adjusted to fill approximately 80% of the CCD dynamic range. Measurements

were acquired with the PT laser on (true poli-OCT signal), PT laser off (background poli-OCT signal), and with the sample arm blocked (noise floor). The poli-OCT signal was calculated as the non-log compressed OCT magnitude signal. Similar to previous work [19, 24], the signal to noise ratio (SNR) was defined as the squared magnitude of the poli-OCT signal with the PT laser on divided by the variance of the image signal with the sample arm blocked. Means and standard deviations were assessed over 10 repeated scans, and statistical significance was calculated using a non-parametric Wilcoxon Rank Sum test ( $p < 0.05$ ).

The integration time of the CCD and the sample arm power were altered individually, and the poli-OCT signal and SNR were calculated and compared to photothermal optical lock-in theory [19] to assess for shot-noise limited performance at millisecond integration times. First, while maintaining the system frequency shift at 500 Hz, the integration time of the CCD ( $\tau = nT_0$ , where  $T_0 = 2$  ms) was increased by integer multiples of the frequency shift period ( $T_0$ ) between 2 ms and 8 ms. For each integration time, the reference arm power was adjusted to fill 80% of the CCD dynamic range. In addition, while maintaining a constant integration time and frequency shift, the SLD power to the sample was increased from 350 to 900  $\mu$ W.

Next, imaging parameters that directly affect the magnitude of the photothermal heating oscillations were altered and trends were compared to approximations of the bio-heat conduction equation [25] as previously reported using traditional PTOCT [11]. The PT laser frequency ( $\Omega_p = \Omega_R$ ) was varied from 200 Hz to 800 Hz while maintaining the integration time of the CCD at 10 ms. Then, the average PT laser power on the sample was varied between 10 and 30 mW. Last, the concentration of ICG in the phantom was varied between 0 and 17  $\mu$ g/ml and imaged with 10 ms CCD integration time, 300 Hz frequency shift, and 30 mW average PT laser power.

Finally, theoretical assumptions of poli-OCT were experimentally validated. According to theory [19], the presence of the photothermal signal in the poli-OCT image requires that the intensity modulation of the PT laser ( $\Omega_p$ ) occurs at the same frequency as the reference arm frequency shift ( $\Omega_R$ ). Therefore,  $\Omega_p$  was varied between 250 Hz and 750 Hz in 50 Hz increments, while maintaining  $\Omega_R$  at 500 Hz. In addition, in order to reject background scattering, the integration time of the CCD ( $\tau$ ) must be set to a multiple of the frequency shift period ( $T_0$ ). To experimentally validate this assumption, while maintaining a constant frequency shift of 500 Hz ( $T_0 = 2$  ms), the integration time was altered from 4 ms ( $\tau = 2T_0$ ) to 8 ms ( $\tau = 4T_0$ ) in 500  $\mu$ s ( $T_0/4$ ) increments.

#### 2.4. Effect of motion and blood flow

All animal studies were approved by the Vanderbilt University Animal Care and Use Committee and meet the NIH guidelines for animal welfare. Transitioning the imaging system to *in vivo* applications requires an understanding of the effects of motion and blood flow on the poli-OCT signal, specifically on the rejection of the background scattering signal (i.e. PT laser off). Therefore, a 4 by 4 mm (400 A-scans/B-scan, 400 B-scans/C-scan) rectangular volume was acquired of a mouse ear (The Jackson Laboratory, Foxn1<sup>nu</sup>/ Foxn1<sup>nu</sup>) using 10 ms CCD integration time, 500 Hz frequency shift, and without the PT laser. A 1 by 1 mm (100 A-scans/B-scan, 100 B-scans/C-scan) rectangular volume was then acquired while varying the reference arm frequency shift ( $\Omega_R$ ) from 100 to 2500 Hz. During imaging, the mouse was anesthetized using inhalant isoflurane (1.5-1.75%) while a closed-loop heating blanket maintained body temperature at 37 degrees Celsius.

#### 2.5. In vivo imaging with poli-OCT

Photothermal imaging was performed *in vivo* in female nude mice (The Jackson Laboratory, Foxn1<sup>nu</sup>/ Foxn1<sup>nu</sup>) using poli-OCT. Mice were anesthetized during imaging using inhalant isoflurane (1.5-1.75%), and a closed-loop heating blanket maintained body temperature at 37 degrees Celsius. Contrast agents were imaged from within intradermal locations of the mouse ear, an optically accessible biological site for preclinical studies of cancer [26], immune response [27, 28], and lymphatics [29–31]. The mouse ear was firmly attached to a 10 ml scintillation vial using double sided tape which was in turn taped to the imaging stage. *En face*

projections were created by taking the average signal across the depth dimension (~1 mm depth).

In the first demonstration of *in vivo* poli-OCT imaging to date, the lymphatic vessels of a healthy mouse ear were imaged with injected ICG in real time. Using a micromanipulator under OCT image guidance, a 31 gauge needle (Hamilton) was placed intradermally in the outer rim of the mouse ear. Approximately 5  $\mu$ l of 500  $\mu$ g/ml ICG [31, 32] was injected, and removal of ICG from the interstitial space via lymphatic vessel drainage was imaged with a 3 by 3 mm (300 A-scans/B-scan, 300 B-scans/C-scan) rectangular volume medial to the injection site. An integration time of 6 ms was used, with 500 Hz frequency shift ( $\Omega_p = \Omega_R$ ), and 30 mW of average PT laser power (770 nm) on the sample. Image volumes were acquired with the PT laser on, the PT laser off, and the frequency shift ( $\Omega_R$ ) set to 0 Hz (i.e. OCT). An accompanying speckle variance scan was acquired to identify native blood vessels over the 3 mm by 3 mm scan window. Speckle variance was calculated as the variance of the OCT magnitude signal over 10 repeated A-scans, acquired at a 10 kHz line rate [17].

Last, similar to previous publications [11], subcutaneous injections of gold nanorods were imaged with poli-OCT. Gold nanorods were manufactured and coated in poly(ethylene glycol) (PEG) according to previous methods [17], diluted to 400 pM concentration in water, then mixed 1:1 with Matrigel (Corning) to a final concentration of 200 pM. The Matrigel-gold nanorod solution was manually injected into the base of a mouse ear using a 28 gauge needle and allowed to solidify for 10 minutes. A 2.5 by 2.5 mm rectangular volume (250 A-scans/B-scan, 250 B-scans/C-scan) was imaged at the periphery of the injection site using 10 ms integration time, 500 Hz frequency shift ( $\Omega_p = \Omega_R$ ), and 35 mW average PT laser power (740 nm) at the sample. Image volumes were captured with the PT laser on and off, and then again with a frequency shift ( $\Omega_R$ ) of 0 Hz. In a separate mouse, a control injection using Matrigel diluted 1:1 in water was imaged using identical image parameters. In addition, an overlapping speckle variance scan was acquired to identify native blood vessels. For *in vivo* imaging, output poli-OCT image volumes were median filtered in the *en face* dimension to reduce the effects of motion artifact and then average filtered. The poli-OCT image contrast was also adjusted to exclude signals near the noise floor, and contrast adjustments were kept consistent across each set of images.

### 3. Results

#### 3.1. Imaging scattering phantoms

Tissue-mimicking phantoms containing ICG (8  $\mu$ g/ml) and TiO<sub>2</sub> were imaged under variable system parameters to quantify poli-OCT performance and to optimize the system for *in vivo* imaging. ICG phantoms did not exhibit significant photobleaching after repeated measurements in the same phantom location, and the phantoms maintained their integrity over multiple months. Results were acquired for the poli-OCT signal with the PT laser on (PT laser (+)), the background signal with the PT laser off (PT laser (-)), and the noise floor with the sample arm blocked. Both the poli-OCT signal (black,  $r^2 = 0.97$ , Fig. 2(a)) and SNR ( $r^2 = 0.97$ , Fig. 2(b)) scaled linearly with the integration time of the CCD while the integration time was set to a multiple of the frequency shift period. The poli-OCT signal scaled with the square root of the sample arm power (black,  $r^2 = 0.98$ , Fig. 2(c)), while the SNR of the poli-OCT signal increased linearly with the sample arm power ( $r^2 = 0.98$ , Fig. 2(d)). The trends observed in Fig. 2 agree with the theory established for photothermal optical lock-in [19], while the trends in SNR agree with the theory for shot noise limited performance, the optimal operation mode for OCT systems [19, 24].



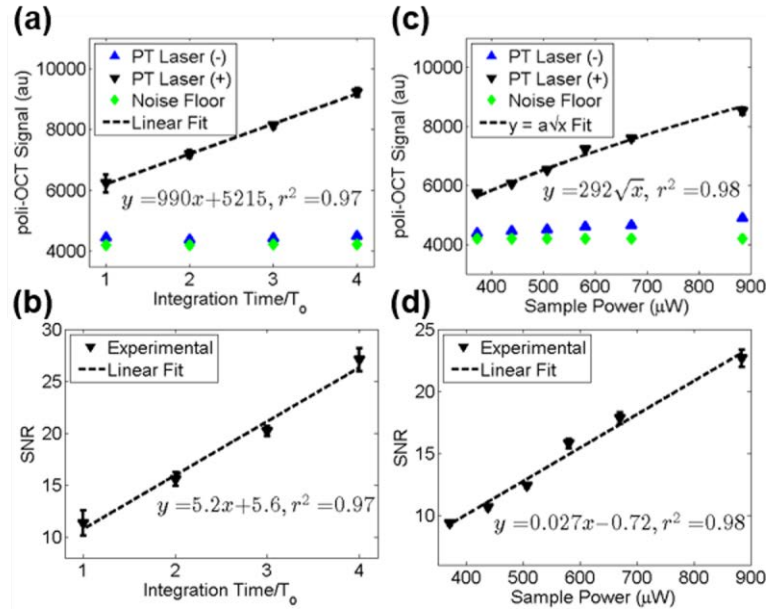


Fig. 2. Poli-OCT signal characterization in phantoms containing ICG (absorber) and  $\text{TiO}_2$  (scatterer) while altering image system parameters. Solid phantoms were imaged with the PT laser on (black, top), the PT laser off (blue, top), and the sample arm blocked (green, top). (a) The poli-OCT signal (black) increased linearly with integration time ( $\tau$ ) set to multiples ( $n$ ) of the frequency shift period ( $T_0$ ). (b) The SNR of the poli-OCT signal increased linearly as well. (c) The poli-OCT signal (black) increased with the square root of the sample arm power, while (d) the SNR increased linearly. The poli-OCT signal agrees with theory [19], and SNR results are consistent with shot noise limited performance [19, 24].

Parameters that affect the magnitude of the photothermal oscillations were also examined. Increasing the PT laser frequency ( $\Omega_P = \Omega_R$ ) from 200 to 800 Hz caused a nonlinear decay in the poli-OCT signal (Fig. 3(a)), while increasing the PT laser power resulted in a linear increase in poli-OCT signal (Fig. 3(b),  $r^2 = 0.99$ ). Scattering phantoms with varying ICG concentrations from 0 to 17  $\mu\text{g/ml}$  displayed a linear increase in poli-OCT signal (Fig. 3(c),  $r^2 = 0.99$ ). Results in Fig. 3(c) include the removal of background signal (PT laser (-)) from the poli-OCT signal (PT laser (+)). Concentrations of ICG as low as 1  $\mu\text{g/ml}$  displayed significantly increased ( $p < 0.05$ , Fig. 3(c) inset) poli-OCT signal compared with scattering controls (red). ICG concentrations greater than 1  $\mu\text{g/ml}$  can be reached at a tumor site when ICG is tagged to a systemically injected antibody, indicating that ICG and poli-OCT could potentially be used for *in vivo* molecular imaging studies in cancer, or to track delivery of antibody therapies (e.g. trastuzumab in breast cancer) [33]. The effects seen from increased PT laser frequency, PT laser power, and absorber concentration all agree with previous traditional PTOCT data and a model of the bio-heat conduction equation [11, 25].

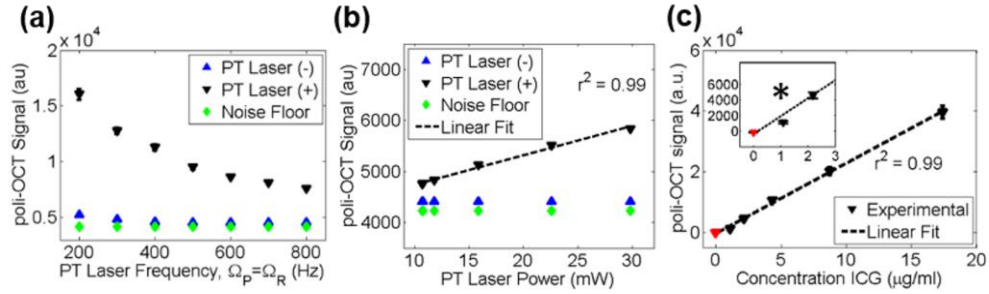


Fig. 3. Poli-OCT signal characterization in phantoms containing ICG (absorber) and  $\text{TiO}_2$  (scatterer) while altering photothermal signal magnitudes. (a) As the PT laser frequency ( $\Omega_p$ , where  $\Omega_p = \Omega_R$ ) is increased, the poli-OCT signal (black) decreases nonlinearly. (b) Increasing PT laser power caused a linear increase in poli-OCT signal. (c) Increasing the concentration of the ICG resulted in a linear increase in the poli-OCT signal. The average signal from  $n = 10$  repeated scans showed a significant increase ( $*p < 0.05$ , figure inset) with  $1 \mu\text{g/ml}$  concentration of ICG compared to the control (red).

Theoretical assumptions for photothermal optical lock-in were experimentally validated as well. Mismatch between the PT laser modulation frequency ( $\Omega_p$ , Fig. 4(a) x-axis) and the reference arm frequency shift ( $\Omega_R$ , Fig. 4(a) red vertical line) caused a large falloff in poli-OCT signal (Fig. 4(a)). There is however, a broad range of frequencies over which the poli-OCT signal remains high (FWHM  $\sim 150$  Hz), indicating that  $\Omega_p$  and  $\Omega_R$  do not need to be precisely frequency locked to measure photothermal absorption. It should be noted that mismatching  $\Omega_p$  and  $\Omega_R$  resulted in temporal oscillations in the image signal (data not shown). Additionally, altering the integration time from 4 ms to 8 ms while maintaining a frequency shift of 500 Hz ( $T_0 = 2$  ms) altered both the poli-OCT signal (PT laser (+), black, Fig. 4(b)) and background scattering signal (PT laser (-), blue, Fig. 4(b)). The poli-OCT background signal (PT laser (-), blue, Fig. 4(b)) approached the noise floor (Noise Floor, green, Fig. 4(b)) only when CCD integration times ( $\tau$ ) were integer multiples ( $n$ ) of the frequency shift period ( $T_0$ ) (Fig. 4(b), red vertical lines). Therefore, any source of alteration to the programmed frequency shift ( $\Omega_R$ ) in the signal could result in incomplete removal of static background scatterers from the poli-OCT image. Slight differences between background and noise floor were due to the autocorrelation signal.

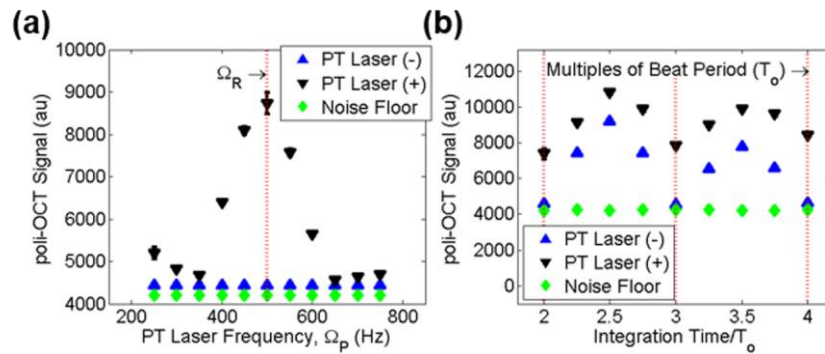


Fig. 4. Poli-OCT signal characterization in phantoms containing ICG (absorber) and  $\text{TiO}_2$  (scatterer), validating theoretical assumptions. (a) When the PT laser modulation frequency ( $\Omega_p$ , x-axis) is mismatched from the reference arm frequency shift ( $\Omega_R$ , red vertical line), the poli-OCT signal (black) is attenuated. (b) The poli-OCT signal with the PT laser on (black) and off (blue) are both minimized at CCD integration times ( $\tau$ ) that are integer multiples ( $n$ ) of the frequency shift period ( $T_0$ ) (red vertical lines). The scattering signal (blue) is effectively removed only when the integration time is equal to a multiple of the frequency shift period.

### 3.2. Effect of motion and blood flow

As demonstrated by phantom experiments (blue, Fig. 4(b)), a false positive background signal emerges when the CCD integration time is not divisible by the frequency shift period. Motion artifact and blood flow expected during *in vivo* imaging impose their own frequency shifts on the image signal, causing the interference pattern to carry a frequency shift different from the programmed one ( $\Omega_R$ ). Therefore, it was hypothesized that motion artifact and blood flow would cause incomplete rejection of a non-absorbing sample. As predicted, motion artifacts due to breathing and cardiac cycles of the mouse as well as blood flow within vessels result in incomplete rejection of the background scattering signal (Fig. 5(a)). Although the background signal due to blood flow and motion seem indistinguishable in one B-scan (Fig. 5(a)), the *en face* average intensity projection from the complete image volume (Fig. 5(b)) reveals the transient and streaking features of the motion artifact (red arrows, Fig. 5(a)-5(b)), and the more structured nature of the flow signal (green arrows, Fig. 5(a)-5(b)). Motion artifact-induced streaking was reduced with a median filter in the *en face* dimension over a 4X4 pixel neighborhood. The filter maintains the structure of the flow found in the vessels, while attenuating streaking artifacts in the image (Fig. 5(c)). The overall background signal (i.e. average image signal with the PT laser off) including movement and blood flow from *in vivo* imaging can be further attenuated by increasing the frequency shift in the reference arm ( $\Omega_R$ , Fig. 5(d)). Increased photothermal frequency ( $\Omega_R$ ) results in both reduced background signal and reduced photothermal signal strength (Fig. 3(a)). Therefore, the photothermal frequency must be carefully selected for each *in vivo* application.

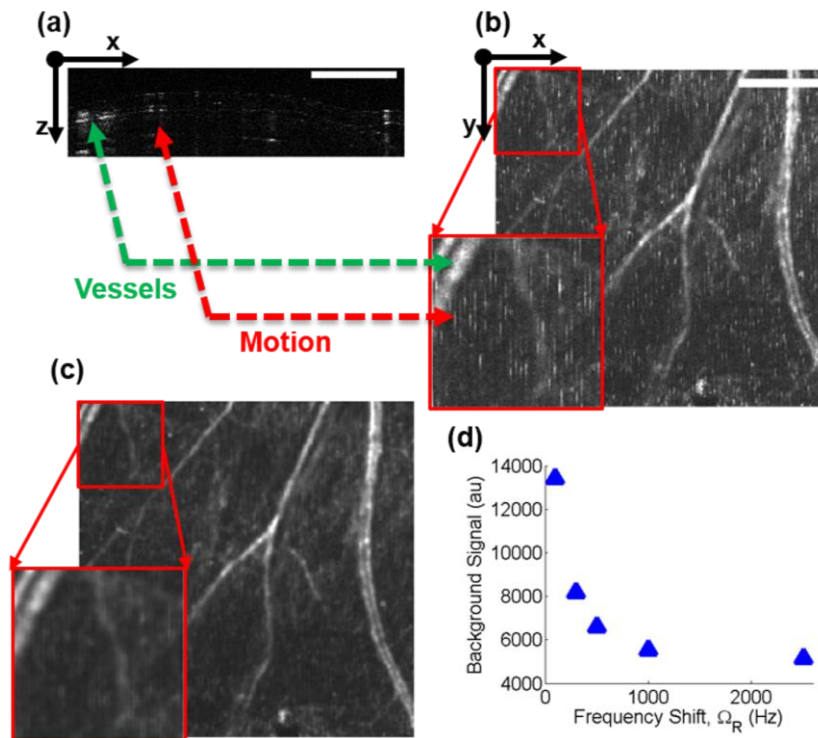


Fig. 5. Motion and blood flow affects *in vivo* poli-OCT signal. A 3D image volume of a mouse ear with the PT laser off shows motion artifact and flow manifested as poli-OCT background signal. (a) A representative B-scan shows false positive background signal due to blood flow in vessels (green arrow) and motion artifact (red arrow). (b) The same image volume represented as an *en face* projection shows the signals due to motion artifact and flow. (c) Median filtering the 3D image volume attenuates artifacts due to motion. (d) The average background signal in the image volume is attenuated with increasing frequency shifts in the reference arm ( $\Omega_R$ , x-axis). Red boxes show 2X zoomed image regions. Scale bar = 1 mm.

### 3.3. *In vivo* imaging with poli-OCT

Recently, ICG has been used as a lymphatic imaging contrast agent due to its bright NIR fluorescence and efficient lymphatic removal [31, 32]. Therefore, as a demonstration of *in vivo* poli-OCT, ICG was imaged from within the lymphatics during its removal from the mouse ear. B-scans through the mouse ear include OCT (gray) and poli-OCT (green) data (Fig. 6(a), 6(b)). Morphological features are resolved through the full thickness of the ear in the OCT magnitude data (Fig. 6(a), 6(b)), and the lymphatics that drain the interstitial ICG are resolved in the poli-OCT data with the PT laser on (Fig. 6(b)). The high concentration of injected ICG (500  $\mu\text{g/ml}$ ) is similar to previous fluorescence based studies [31, 32] making the poli-OCT signal extremely bright. The network structure of the lymphatics is more evident when visualizing the *en face* average intensity projection of the image volume (Fig. 6(c), 6(d)). With the PT laser off, the background signal (green, Fig. 6(c)) overlaps only with the location of blood vessels identified by speckle variance OCT (red, Fig. 6(c)), as predicted by results found in Fig. 5. With the PT laser on, the poli-OCT signal identifies the lymphatic vascular networks removing ICG from the intradermal injection site towards the base of the ear (green, Fig. 6(d)). The green circular feature at the bottom of Fig. 6(d) corresponds to a surface leak of the ICG near the injection site.

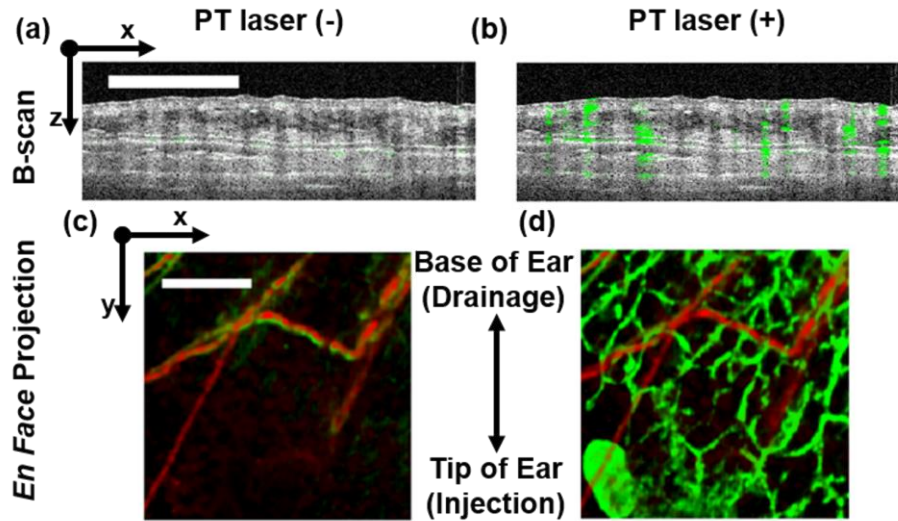


Fig. 6. *In vivo* poli-OCT of mouse ear lymphatics using ICG as a contrast agent. 3D image volumes were acquired of a mouse ear after intradermal injection of ICG. Representative B-scans containing tissue morphology (gray) and poli-OCT signal (green) with the PT laser (a) off and (b) on. (c) *En face* projections of the volume including the vasculature (red, speckle variance OCT) shows minimal extravascular poli-OCT signal (green) with the PT laser off. (d) With the PT laser on, the poli-OCT signal (green) increases in locations where the lymphatic vessels are draining ICG from the injection site. Scale bar = 1 mm.

To demonstrate the breadth of potential imaging contrast agents for poli-OCT, gold nanorods were also imaged *in vivo* at 10 times faster frame rates than previously reported for *in vivo* imaging of similar concentrations of gold nanorods using traditional PTOCT [11]. Injections of either Matrigel alone or Matrigel with 200 pM of gold nanorods were imaged over 2.5 mm by 2.5 mm volumes with poli-OCT (green, Fig. 7). Overlapping speckle variance OCT scans identified the locations of blood vessels (red, Fig. 7). After injection of Matrigel alone into the mouse ear, *en face* average intensity projections revealed no significant extravascular poli-OCT signal with either the PT Laser off (Fig. 7(a)) or the PT Laser on (Fig. 7(b)). Additionally, after gold nanorod injections into the mouse ear, there were no extravascular regions of poli-OCT signal with the PT Laser off (Fig. 7(c)). However, a

significantly enhanced poli-OCT signal was present in the region surrounding the site of gold nanorod-loaded Matrigel injection (Fig. 7(d)). Unlike the ICG lymphatic imaging (Fig. 6), the gold nanorods remained localized near the injection site due to the solidification of the Matrigel at body temperature.

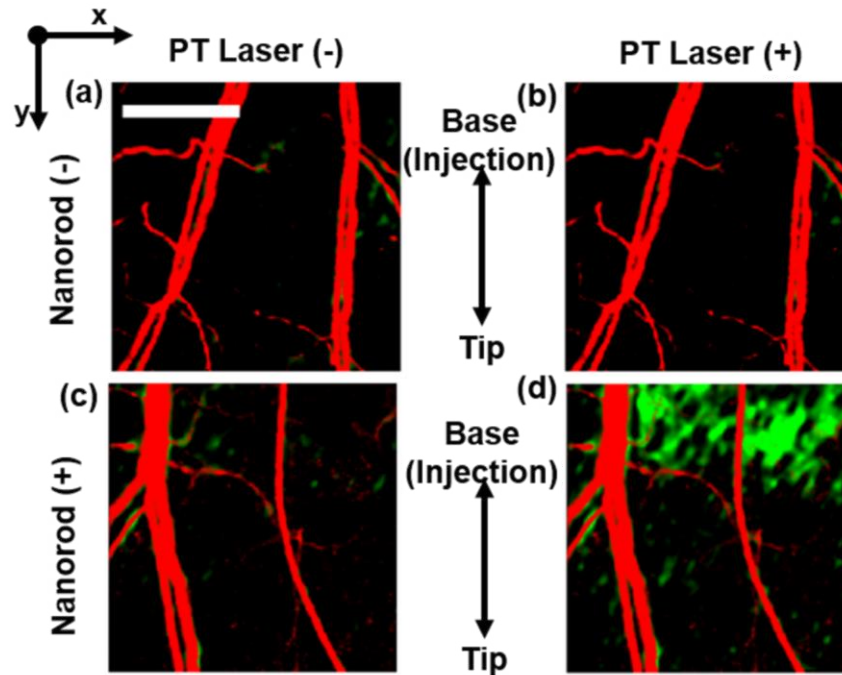


Fig. 7. *In vivo* poli-OCT imaging of subcutaneous injections of gold nanorods in two mice. 3D image volumes were acquired of a mouse ear after injection of Matrigel alone (top) or Matrigel plus 200 pM gold nanorods (bottom). *En face* average intensity projections contain the poli-OCT signal (green) and speckle variance OCT signal (red). With Matrigel alone, no poli-OCT signal is observed (a) without or (b) with the PT laser. (c) In the presence of gold nanorods, no extra-vascular poli-OCT signal is present without the PT laser. (d) Only with gold nanorods and the PT laser on, is there an observable poli-OCT signal. Scale bar = 1 mm.

#### 4. Discussion

We have incorporated optical lock-in methods into traditional PTOCT, and for the first time demonstrated *in vivo* poli-OCT. The poli-OCT system and signal was characterized while imaging tissue-mimicking phantoms containing an FDA-approved small molecule fluorophore (ICG). We also assessed how motion artifact and blood flow, confounding factors unique to *in vivo* imaging, affect the background signal in poli-OCT. Finally, two contrast agents were imaged *in vivo*, demonstrating the versatility of poli-OCT for use with small molecule and nanoparticle contrast agents. The ability to image fluorophores common to molecular imaging [34] as well as gold nanoparticles under development for molecular imaging and drug delivery [35] demonstrates the breadth of potential poli-OCT applications. Given the improvements enabled by poli-OCT, the unique spatial imaging niche of OCT, and the range of potential contrast agents available for imaging, the optical lock-in techniques demonstrated in these studies could enable more widespread adoption of photothermal OCT for *in vivo* imaging.

In this study, poli-OCT was used to identify gold nanorods in real time at ten times faster frame rates and with 1000 times less digital data acquisition than a previous PTOCT study (Fig. 7 and [11]). The previous PTOCT study from our group imaged 400 pM gold nanorods subcutaneously injected into the mouse ear (2X higher concentration than the current study)



using 200 Hz photothermal laser modulation frequency, 3.2 kW/cm<sup>2</sup> average irradiance, and 100 ms observation time at each A-scan position. In the current study, a photothermal modulation frequency of 500 Hz was used to avoid background signal contribution (Fig. 5(d)), and the average irradiance was increased to 15.5 kW/cm<sup>2</sup> to account for the signal decrease at faster modulation frequencies (Fig. 3(a)). Even with increased irradiance, the tenfold increase in poli-OCT imaging speed reduced the total radiant exposure at each A-scan position by a factor of two, from 320 J/cm<sup>2</sup> in the previous PTOCT study [11] to 155 J/cm<sup>2</sup> in the current poli-OCT study. To better understand the impact of these advances for *in vivo* imaging studies, scan length times and data burden were calculated and compared for poli-OCT and traditional PTOCT [11], assuming 1024 pixels per A-scan saved as 16 bit unsigned integers. For each A-scan position, poli-OCT acquired one A-scan over 10 ms, while a previously reported traditional PTOCT system acquired 1000 A-scans over 100 ms [11]. For a study including 10 mice imaged over a 300 by 300 rectangular scan volume repeated at five time points, the previously reported PTOCT system would require 7500 minutes (125 hours) and 9.2 TB of data acquisition, while poli-OCT would require only 750 total minutes (12.5 hours) and 9.2 GB of data acquisition. Thus, poli-OCT provides more streamlined *in vivo* time-course studies than previously reported PTOCT systems. GPU processing [36] could also be used to mitigate the data acquisition and offline signal analysis burden of traditional PTOCT, and offers reduced optical complexity compared to poli-OCT. However, previous publications that implement the optical lock-in detection scheme used in poli-OCT have suggested significant SNR improvements over digital sampling of phase modulations [20], an advantage that GPU processing of traditional PTOCT data does not provide. Nevertheless, this paper demonstrates the first real time *in vivo* PTOCT images, at increased frame rates compared to previous publications that use traditional PTOCT to image similar samples [11, 17].

While this work demonstrates improvements of poli-OCT with respect to traditional PTOCT, the current poli-OCT design includes a few addressable shortcomings. The technical advancement from traditional PTOCT to poli-OCT has increased the complexity of the optical instrumentation. For example, the use of three AOMs to control the reference arm frequency shift ( $\Omega_R$ ) and photothermal laser intensity modulation ( $\Omega_p$ ) increases the cost and complexity over traditional PTOCT. AOMs are attractive for this application because they provide both frequency shifting and amplitude modulation, can be phase and frequency locked to each other, and supply a wide range of frequencies. However, as demonstrated in Fig. 4(a), precise frequency matching of  $\Omega_p$  and  $\Omega_R$  may not be required for poli-OCT, so approaches that are less precise but more cost effective than AOMs could be implemented (e.g. moving reference arm [37], offset scanning reference mirror [38]). An additional source of poli-OCT imaging system complexity is the one way optical paths in both the reference and sample arms, which are used to reduce unwanted back-reflections acquired during long CCD acquisition times. Long CCD acquisition times are governed by the photothermal laser modulation frequency ( $\Omega_p$ ), which is slow due to the inverse relationship between photothermal signal magnitude and photothermal laser modulation frequency (Fig. 3(b) and [11]). Furthermore, for *in vivo* poli-OCT, focusing optics with a larger depth of focus and correspondingly larger spot sizes than microscopy are desirable. These larger spot sizes require slower photothermal modulation frequencies (e.g. hundreds of Hz) than photothermal microscopy for optimal performance [18, 39]. Photothermal modulation frequencies ( $\Omega_p$ ) in the hundreds of Hz regime require millisecond CCD integration times (e.g. if  $\Omega_R = \Omega_p = 500$  Hz,  $\tau \geq 2$  ms). One-way optical paths help to reduce unwanted back-reflections that can consume a large portion of the CCD dynamic range at these long integration times.

In comparison to traditional PTOCT and OCT, poli-OCT requires additional unique considerations. First, the contribution of certain image signals is greatly enhanced in poli-OCT images compared to OCT. The poli-OCT cross-correlation signal due to photothermal heating is an attenuated version of the original OCT cross-correlation signal. However, the poli-OCT autocorrelation signal is not frequency shifted and therefore not attenuated compared to the original OCT image. Consequently, the intensity of the autocorrelation signal

relative to the cross-correlation signal is large for poli-OCT compared to traditional PTOCT or OCT. In this work, the poli-OCT autocorrelation signal was attenuated using cross-polarized sample arm light that limited surface specular reflections [40–42]. Furthermore, the autocorrelation image remains largely unchanged with or without the PT laser, and therefore subtracting an image with the PT laser off from an image with the PT laser on can help minimize the autocorrelation signal and generate images with minimal artifact. Note that this was not required for these *in vivo* imaging applications (Fig. 6 and Fig. 7). In addition to the autocorrelation signal effects, the poli-OCT signal depends on the reflectivity of the sample and reference arms (Eq. (1) [19]. Therefore, variations in image parameters or tissue optical properties can affect images taken on different days or between samples. Dividing the poli-OCT image by the OCT image ( $\Omega_R = 0$ ) can account for day-to-day inter-sample and intra-sample variations in reflectivity, and aid in maximizing contrast in the poli-OCT signal. If OCT images are desired in addition to poli-OCT images, an OCT scan must be acquired separately from the poli-OCT scan. However, the OCT data can be captured at significantly faster integration times than poli-OCT, thus minimally affecting overall acquisition time. A remaining consideration is phase accumulation, or the integration of the PTOCT signal with depth [43]. Unlike traditional PTOCT, the poli-OCT signal is also a function of the OCT signal magnitude (Eq. (1). Therefore, phase accumulation does occur, but the signal first increases with depth due to phase accumulation then decreases with depth due to OCT signal falloff (data not shown). Algorithms are currently under development to address this issue.

In conclusion, for the first time, we have demonstrated *in vivo* poli-OCT for real time imaging of both small molecules and gold nanoparticles. Using poli-OCT, PTOCT data can be acquired faster, with orders of magnitude less data burden, and real time signal analysis. Mitigating the slow acquisition and high data burden of traditional PTOCT gives poli-OCT the potential to significantly impact preclinical *in vivo* molecular imaging. Higher volume acquisition rates and real time display of photothermal images could enable *in vivo* PTOCT applications that are not feasible with traditional PTOCT, such as time-course tomograms of small molecule drug delivery [4]. In addition, poli-OCT is attractive for other applications where the high resolution, wide field of view, and accompanying label-free imaging of tissue and vessel morphology provide significant advantages over traditional imaging techniques. Potential applications are numerous: molecular imaging in mammary, dorsal, abdominal, and cranial window models of cancer [34]; noninvasive imaging of drug delivery kinetics to assess the impact of drug vector size [44, 45], surface chemistry [46], and shape [47]; imaging drug clearance [48]; and imaging local drug diffusion and release [49, 50]. Overall, by leveraging the existing high resolution and wide field of view of OCT as well as its abilities to image tissue and vessel morphology, poli-OCT holds significant promise in studies of drug discovery and drug delivery, molecular imaging, and biological studies of pathogenesis.

## Acknowledgments

This work was supported by grants from the National Institutes of Health under award numbers R00CA142888 and R25CA136440. The authors would like to thank Kelsey R. Beavers and Dr. Craig L. Duvall for supplying gold nanorods.